Vectors to ore in replacive VMS deposits of the northern Iberian Pyrite Belt: mineral zoning, whole rock geochemistry, and use of portable XRF

Guillem Gisbert[1], Fernando Tornos[1], Emma Losantos[1], Juan Manuel Pons[2], Juan Carlos Videira[2]

[1] Institute of Geosciences (CSIC-UCM), Madrid, 28040, Spain
[3] MATSA, Almonaster la Real, Huelva, 21342, Spain

SUPPLEMENTARY MATERIALS 1

S1.1 Geology of the Iberian Pyrite Belt

Formation of the IPB VMS district is related to the geodynamic evolution leading to the growth of the Variscan orogen in the southern Iberian Peninsula during late Paleozoic. The IPB belongs to the southernmost domain of the Variscan Belt in the Iberian Peninsula, the South Portuguese Zone (Julivert et al., 1974), which was accreted by north-directed subduction below the Autochthonous Iberian Terrane (Munhá et al., 1986; Quesada and Ribeiro, 1988; Ribeiro et al., 1990; Silva et al., 1990; Quesada, 1991; Oliveira and Quesada, 1998). The stratigraphic sequence of the IPB records the pre-, syn-, and post-collisional evolution of the northern continental margin of South Portuguese Zone terrane. It consists of a relatively simple 1000-5000 m thick (base not exposed; Tornos, 2006) Devonian to Carboniferous (Oliveira, 1990; Oliveira et al., 2004) sequence which has been divided into three main units (Schermerhorn, 1971), from older to younger: 1) Phyllite-Quartzite Group (PQ), 2) Volcanic Sedimentary Complex (VSC), which hosts the mineralization, and 3) Culm Group or Baixo Alentejo Flysch Group.

From Frasnian (?) to Late Fammenian times interbedded quartz sandstones and shales were deposited in a stable and shallow epicontinental platform (most of the PQ Group) (Moreno et al., 1996). In the Late Fammenian, a transtensional regime related to the left-lateral northwards oblique collision of the South Portuguese Zone with the autochthonous Iberian terranes generated pull-apart basins with lowered, tilted and uplifted blocks that subdivided the depositional environment into several mainly E-W-trending sub-basins separated by shallow marine to subaerial areas (Silva et al., 1990; Moreno et al., 1996; Sáez et al., 1996; Quesada, 1991; Oliveira et al., 2004; Tornos et al., 2005). Decompression-induced mantle partial melting related to crustal thinning generated mafic magmas that underplated and intruded the continental crust promoting its partial melting and the generation of hot dry felsic magmas (Munhá, 1983; Mitjavila et al., 1997; Thiéblemont et al., 1997). Magmatism in the IPB is strongly bimodal consisting of: 1) mantle-derived mafic rocks of dominant continental tholeiitic character and minor local intraplate alkaline characteristics; 2) crustally-derived felsic rocks; 3) minor intermediate composition magmas interpreted to represent either mixtures of the two dominant magma populations or mafic magmas modified by assimilation of crustal rocks (Munhá, 1983; Mitjavila et al., 1997; Thieblemont et al., 1997). From Late Famennian to early Late Visean, mantle-derived mafic magmas and crustal felsic magmas reached the surface producing a complex bimodal volcanic and shallow intrusive sequence interbedded with mudstone and some chemical sediments (VSC). Felsic rocks mostly occur as dome(-cryptodome) complexes, with less volcaniclastic materials (hialoclastic, pyroclastic, epiclastic), and intrusions (sills) (Boulter, 1993; Soriano and Martí, 1999; Rosa et al., 2008, 2009, 2010; Conde and Tornos, 2019), although sills may be locally abundant (e.g. in the Rio Tinto and Tharsis areas; Boulter, 1993; Tornos et al., 1998; Soriano and Martí, 1999). Mafic rocks are dominantly cohesive occurring mainly as basaltic sills or small stocks, less as submarine lava flows with local pillow lavas, and more rarely as volcaniclastic deposits (García Palomero, 1980; Boulter, 1993; Soriano and Martí, 1999; Rosa et al., 2008, 2009, 2010; Conde and Tornos, 2019). Crustal thinning and magmatic intrusion triggered the hydrothermal

circulation responsible for the massive sulphide mineralizing events (Oliveira, 1990; Oliveira et al., 2004; Mitjavila et al., 1997; Tornos, 2006). In the Late Visean the tectonic setting shifted to compressional related to the main collisional stage of the Variscan orogeny in the area (Quesada, 1998). This formed a south-ward propagating foreland basin in which syn-orogenic flysch sediments (Culm Group) were deposited (Oliveira, 1990; Silva et al., 1990, Quesada, 1998).

Compressive tectonism in the IPB lasted from Late Visean to Late Moscovian (Oliveira et al., 1979; Silva et al., 1990; Pereira et al., 2008). The stratigraphic record of the IPB was disrupted forming a S (Spain) and SW (Portugal)-verging and -propagating thin-skinned foreland fold and thrust belt (Ribeiro and Silva, 1983; Silva et al., 1990; Quesada, 1991, 1998). In the Spanish sector of the IPB this deformational structure is interpreted to consist of an over 150 km long and 10-15 km thick imbricated fan-like system formed by several piled up tectonic units less than 2 km thick (Quesada, 1991, 1998; Alonso et al., 1999; Soriano and Casas, 2002) where the main structures seem to be controlled by previous extensional faults and rheological contrasts (Quesada, 1998; Mantero et al., 2011; Martin-Izard et al., 2016). Deformation involved pervasive reactivation and inversion of prior extensional structures, and mainly produced asymmetric folds verging to the S and SW, with long normal limbs and short overturned limbs which can be intersected or supressed by thrusts, resulting in a stacking of mainly normal limbs (Silva et al., 1990; Quesada, 1991, 1998; Mantero et al., 2011). Local back-thrusts and lateral ramps add complexity to the structure (Quesada, 1998; Mantero et al., 2011). Penetrative foliation developed mostly parallel to axial planes but also transecting them due to a transpressional regime (Ribeiro et al., 1983; Simancas, 1983; Quesada, 1998), with zones of intense mylonitic foliation associated to both thrusts and lateral ramps (Quesada, 1998).

Low-grade regional metamorphism, from prehnite-pumpellyite to low green schist facies, affected rocks in the IPB during the main collisional stage of the Variscan orogeny (Schermerhorn, 1975; Munhá, 1979, 1983, 1990, Sánchez España, 2000). Deformation and metamorphic grade of exposed rocks tend to increase from south to north (Ribeiro and Silva 1983; Munhá, 1990), although a general metamorphic gradient is not clearly marked. Instead, zones of locally enhanced deformation and metamorphic grade occur in proximity to high strain zones (e.g. shear zones) (Sáez et al., 1996; Sánchez España, 2000; Sánchez España et al., 2000).

Significant variations in the composition of the VSC sequence across the IPB lead several authors to subdivide the IPB into major E-W oriented domains characterized, among other factors, by different abundances in volcanic materials and the composition of the sedimentary fraction (e.g. Routhier et al., 1978; Quesada, 1996; Sáez et al.,1999). In general terms, most classifications separate a northern domain in which the VSC is dominated by volcanic materials with minor fine-grained sediments with limited continental influence, and a southern domain dominated by shales and siliciclastic sediments with continental influence and minor volcanic and subvolcanic materials.

Two main contrasting styles of VMS mineralization have been described in the IPB which are closely related to the nature of the host stratigraphic sequence: shale-hosted and felsic-volcanic-rocks-hosted deposits (Tornos, 2006; Tornos et al., 1998, 2008, 2015; Tornos and Conde, 2002; Tornos and Heinrich, 2008; Velasco-Acebes et al., 2019).

Shale-hosted deposits. They are interpreted to have formed mainly by exhalative processes in sub-oxic to anoxic third order basin seafloor where upwelling deep sulphur-depleted fluids mixed with modified seawater rich in biogenically reduced sulphur, leading to the precipitation of the massive sulphides on the seafloor. Shale-hosted deposits share features such as: intermediate to high aspect ratio (typically 10 to 20), usually larger tonnages, stratiform morphology, absence of major metal refining, abundance of sedimentary structures, absence of sulphates, and common presence of siderite-rich facies. This type of deposit dominates in the southern IPB, and example deposits are: Sotiel-Migollas, Tharsis, Lousal, Las Cruces, Aznalcóllar-Los Frailes or Masa Valverde.

Felsic volcanic rocks-hosted deposits. They are interpreted to have formed mainly by stratabound replacement of porous or reactive massive and volcaniclastic (vitriclast- or pumice-rich) volcanic rocks during mixing of the deep sulphur-poor fluids with modified seawater bearing variably reduced sulphur acquired from leaching of the host volcanic rocks or by thermochemical reduction of the marine sulphate. These deposits share features such as: sharp transgressive contacts with the host rocks, presence of a pervasive wrapping hydrothermal alteration, variable aspect ratio, major metal refining, and abundance of sulphates. They usually have lower tonnages than shale-hosted exhalative ones, but higher base metal contents. This type of deposit dominates in the northern IPB, and example deposits are: Aguas Teñidas, La Zarza, Aljustrel, Concepción, or La Magdalena.

In the Rio Tinto area, which is geographically and lithologically transitional, both types of mineralization occur.

In addition to the massive sulphides, the IPB also holds numerous stratiform Fe-Mn ores within the VSC (mainly jaspers, which may occur laterally to massive sulphides) and non-economic late vein mineralization within the VSC and Culm Group (interpreted as produced by metal remobilization from the massive sulphides during the late stages of the Variscan orogeny) (Carvalho et al., 1999; McKee, 2003).

References

Alonso, F. M., Garcia Navarro, E., and Camacho, M. A.: Deformación progresiva de la Zona Sudportuguesa: plegamiento y cizallamiento de secuencias multicapa, Geogaceta, 11-14, 1999.

Boulter, C. A.: Comparison of Rio Tinto, Spain, and Guaymas Basin, Gulf of California: An explanation of a supergiant massive sulfide deposit in an ancient sill-sediment complex, Geology, 21, 801-804, 10.1130/0091-7613(1993)021<0801:cortsa>2.3.co;2, 1993.

Carvalho, D., Barriga, F. J. A. S., and Munhá, J.: Bimodal siliciclastic systems - The case of the Iberian Pyrite Belt, in: Volcanic-associated massive sulfide deposits: processes and examples in modern and ancient settings, edited by: Barrie, C. T., and Hannington, M. D., Reviews in Economic Geology, 8, Society of Economic Geologists, 375-408, 1999.

Conde, C. and Tornos, F.: Geochemistry and architecture of the host sequence of the massive sulfides in the northern Iberian Pyrite Belt, Ore Geol. Rev., 127, 103042, https://doi.org/10.1016/j.oregeorev.2019.103042, 2020.

García Palomero, F.: Caracteres geológicos y relaciones morfológicas y genéticas de los yacimientos del anticlinal de Riotinto, PhD Thesis, Instituto de Estudios Onubenses, 263 pp., 1980.

Julivert, M., Fontboté, J. M., Ribeiro, A., and Conde, L.: Mapa tectónico de la Península Ibérica y Baleares, Escala 1:1 000 000, Instituto Geológico y Minero de España, Madrid, 101 pp., 1974.

Mantero, E. M., Alonso-Chaves, F. M., García-Navarro, E., and Azor, A.: Tectonic style and structural analysis of the Puebla de Guzmán Antiform (Iberian Pyrite Belt, South Portuguese Zone, SW Spain), Geological Society, London, Special Publications, 349, 203-222, 10.1144/sp349.11, 2011.

Martin-Izard, A., Arias, D., Arias, M., Gumiel, P., Sanderson, D. J., Castañon, C., and Sanchez, J.: Ore deposit types and tectonic evolution of the Iberian Pyrite Belt: From transtensional basins and magmatism to transpression and inversion tectonics, Ore Geol. Rev., 79, 254-267, https://doi.org/10.1016/j.oregeorev.2016.05.011, 2016.

McKee, G. S.: Genesis and deformation of the Aguas Teñidas Este massive sulphide deposit and implications for the formation, structural evolution and exploration of the Iberian Pyrite Belt, University of Birmingham, 2003.

Mitjavila, J., Martí, J., and Soriano, C.: Magmatic Evolution and Tectonic Setting of the Iberian Pyrite Belt Volcanism, J. Petrol., 38, 727-755, 10.1093/petroj/38.6.727, 1997.

Moreno, C., Sierra, S., and Sáez, R.: Evidence for catastrophism at the Famennian-Dinantian boundary in the Iberian Pyrite Belt, in: Recent advances in Lower Carboniferous geology, edited by: Strogen, P., Somerville, I. D., and Jones, G. L., Special Publications, Geological Society, London, 153-162, https://doi.org/10.1144/GSL.SP.1996.107.01.12, 1996.

Munhá, J.: Blue amphiboles, metamorphic regime and plate tectonic modelling in the Iberian Pyrite Belt, Contrib. Mineral. Petrol., 69, 279-289, 10.1007/bf00372330, 1979.

Munhá, J.: Hercynian magmatism in the Iberian Pyrite Belt, Memórias dos Serviços Geológicos de Portugal, 29, 39-81, 1983.

Munha, J.: Metamorphic Evolution of the South Portuguese/Pulo Do Lobo Zone, in: Pre-Mesozoic Geology of Iberia, edited by: Dallmeyer, R. D., and Garcia, E. M., Springer Berlin Heidelberg, Berlin, Heidelberg, 363-368, 10.1007/978-3-642-83980-1_25, 1990.

Munhá, J., Oliveira, J., Ribeiro, A., Oliveira, V., Quesada, C., and Kerrich, R.: Beja-Acebuches Ophiolite: characterization and geodynamic significance, II Congr Nacion Geol, 29 Sept-2 Oct., Maleo (Bol Inform Soc Geol Port), 2-13, 31, 1986.

Oliveira, J. T.: South Portuguese Zone: introduction. Stratigraphy and synsedimentary tectonism, in: PreMesozoic Geology of Iberia, edited by: Dallmeyer, R. D., and Martínez García, E., Springer Verlag, 333-347, 1990.

Oliveira, J. and Quesada, C.: A comparison of stratigraphy, structure, and palaeogeography of the South Portuguese Zone and southwest England, European Variscides, Geoscience in South- West England, The Scott Simpson Lecture, Annual Conference of the Ussher Society, Proceedings of the Ussher Society, 9, 141-150, 1998.

Oliveira, J. T., Horn, M., and Paproth, E.: Preliminary note on the stratigraphy of the Baixo Alentejo Flysch Group, Carboniferous of Southern Portugal and on the palaeogeographic development, compared to corresponding units in Northwest Germany, Comunicações dos Serviços Geológicos de Portugal, 65, 151-198, 1979.

Oliveira, J. T., Pereira, Z., Carvalho, P., Pacheco, N., and Korn, D.: Stratigraphy of the tectonically imbricated lithological succession of the Neves Corvo mine area, Iberian Pyrite Belt, Portugal, Miner. Depos., 39, 422-436, 10.1007/s00126-004-0415-2, 2004.

Pereira, Z., Matos, J. X., Fernandes, P., and Oliveira, J. T.: Palynostratigraphy and systematic palynology of the Devonian and Carboniferous sucessions of the South Portuguese Zone, Portugal, Memórias do Instituto Nacional de Engenharia Tecnologia e Inovação 34, Instituto Nacional de Engenharia, Tecnologia e Inovação, Lisboa, 181 pp.2008.

Quesada, C.: Geological constraints on the Paleozoic tectonic evolution of tectonostratigraphic terranes in the Iberian Massif, Tectonophysics, 185, 225-245, https://doi.org/10.1016/0040-1951(91)90446-Y, 1991.

Quesada, C.: Estructura del sector español de la Faja Pirítica: implicaciones para la exploración de yacimientos, Boletín Geológico y Minero, 107, 65-78, 1996.

Quesada, C.: A reappraisal of the structure of the Spanish segment of the Iberian Pyrite Belt, Miner. Depos., 33, 31-44, 1998.

Quesada, C. and Ribeiro, A.: Tectonostratigraphic terrane map of the Iberian Massif, in: Tectonic map of pre-Mesozoic terranes in the circum-Atlantic Phanerozoic orogens, edited by: Kepple, J. D., and Dallmeyer, R. D., IGCP Project 233, Terranes in Circum-Atlantic Paleozoic Orogens, Halifax, 1988.

Ribeiro, A. and Silva, J. B.: Structure of South Portuguese Zone, Memórias dos Serviços Geológicos de Portugal, 39, 83-90, 1983.

Ribeiro, A., Quesada, C., and Dallmeyer, R. D.: Geodynamic Evolution of the Iberian Massif, in: Pre-Mesozoic Geology of Iberia, edited by: Dallmeyer, R. D., and Garcia, E. M., Springer Berlin Heidelberg, Berlin, Heidelberg, 399-409, 10.1007/978-3-642-83980-1_28, 1990.

Rosa, C. J. P., McPhie, J., Relvas, J. M. R. S., Pereira, Z., Oliveira, T., and Pacheco, N.: Facies analyses and volcanic setting of the giant Neves Corvo massive sulfide deposit, Iberian Pyrite Belt, Portugal, Miner. Depos., 43, 449-466, 10.1007/s00126-008-0176-4, 2008.

Rosa, D. R. N., Finch, A. A., Andersen, T., and Inverno, C. M. C.: U–Pb geochronology and Hf isotope ratios of magmatic zircons from the Iberian Pyrite Belt, Mineral. Petrol., 95, 47-69, 10.1007/s00710-008-0022-5, 2009.

Rosa, C. J. P., McPhie, J., and Relvas, J. M. R. S.: Type of volcanoes hosting the massive sulfide deposits of the Iberian Pyrite Belt, J. Volcanol. Geotherm. Res., 194, 107-126, https://doi.org/10.1016/j.jvolgeores.2010.05.005, 2010.

Routhier, P.: La Ceinture sud-ibérique à amas sulfurés dans sa partie espagnole médiane: tableau géologique et métallogénique: synthèse sur le type amas sulfurés volcano-sédimentaires, Éditions du Bureau de Recherches Géologiques et Minières, 94, Paris, 265 pp.1978.

Sáez, R., Almodóvar, G. R., and Pascual, E.: Geological constraints on massive sulphide genesis in the Iberian Pyrite Belt, Ore Geol. Rev., 11, 429-451, https://doi.org/10.1016/S0169-1368(96)00012-1, 1996.

Sáez, R., Pascual, E., Toscano, M., and Almodóvar, G. R.: The Iberian type of volcano-sedimentary massive sulphide deposits, Miner. Depos., 34, 549-570, 10.1007/s001260050220, 1999.

Sánchez España, J.: Mineralogía y geoquímica de yacimientos de sulfuros masivos en el área nor-oriental de la Faja Pirítica Ibérica (San Telmo - San Miguel - Peña del Hierro), norte de Huelva, España, PhD Thesis, Universidad del País Vasco, 2000.

Sánchez-España, J., Velasco, F., and Yusta, I.: Hydrothermal alteration of felsic volcanic rocks associated with massive sulphide deposition in the northern Iberian Pyrite Belt (SW Spain), Appl. Geochem., 15, 1265-1290, https://doi.org/10.1016/S0883-2927(99)00119-5, 2000.

Schermerhorn, L. J. G.: An outline stratigraphy of the Iberian Pyrite Belt, Boletín Geológico y Minero, 82, 23-52, 1971.

Schermerhorn, L. J. G.: Spilites, regional metamorphism and subduction in the Iberian Pyrite Belt: some comments, Geologie en Mijnbouw, 54, 23-35, 1975.

Silva, J. B., Oliveira, J. T., and Ribeiro, A.: Structural Outline, in: Pre-Mesozoic Geology of Iberia, edited by: Dallmeyer, R. D., and Garcia, E. M., Springer Berlin Heidelberg, Berlin, Heidelberg, 348-362, 10.1007/978-3-642-83980-1_24, 1990.

Simancas, J. F.: Geología de la extremidad oriental de la Zona Sudportuguesa, PhD Thesis, Universidad de Granada, 439 pp., 1983.

Soriano, C. and Marti, J.: Facies analysis of volcano-sedimentary successions hosting massive sulfide deposits in the Iberian Pyrite Belt, Spain, Economic Geology, 94, 867-882, 10.2113/gsecongeo.94.6.867, 1999.

Soriano, C. and Casas, J.: Variscan tectonics in the Iberian Pyrite Belt, South Portuguese Zone, Int. J. Earth Sci., 91, 882-896, 10.1007/s00531-001-0253-8, 2002.

Thiéblemont, D., Pascual, E., and Stein, G.: Magmatism in the Iberian Pyrite Belt: petrological constraints on a metallogenic model, Miner. Depos., 33, 98-110, 10.1007/s001260050135, 1997.

Tornos, F.: Environment of formation and styles of volcanogenic massive sulfides: The Iberian Pyrite Belt, Ore Geol. Rev., 28, 259-307, https://doi.org/10.1016/j.oregeorev.2004.12.005, 2006.

Tornos, F. and Conde, C.: La influencia biogénica en la formación de sulfuros masivos de la Faja Pirítica Ibérica, Geogaceta, 32, 235-238, 2002.

Tornos, F. and Heinrich, C. A.: Shale basins, sulfur-deficient ore brines and the formation of exhalative base metal deposits, Chem. Geol., 247, 195-207, https://doi.org/10.1016/j.chemgeo.2007.10.011, 2008.

Tornos, F., González Clavijo, E., and Spiro, B.: The Filon Norte orebody (Tharsis, Iberian Pyrite Belt): a proximal low-temperature shale-hosted massive sulphide in a thin-skinned tectonic belt, Miner. Depos., 33, 150-169, 10.1007/s001260050138, 1998.

Tornos, F., Casquet, C., and Relvas, J. M. R. S.: 4: Transpressional tectonics, lower crust decoupling and intrusion of deep mafic sills: A model for the unusual metallogenesis of SW Iberia, Ore Geol. Rev., 27, 133-163, https://doi.org/10.1016/j.oregeorev.2005.07.020, 2005.

Tornos, F., Peter, J. M., Allen, R., and Conde, C.: Controls on the siting and style of volcanogenic massive sulphide deposits, Ore Geol. Rev., 68, 142-163, https://doi.org/10.1016/j.oregeorev.2015.01.003, 2015.

Velasco-Acebes, J., Tornos, F., Kidane, A. T., Wiedenbeck, M., Velasco, F., and Delgado, A.: Isotope geochemistry tracks the maturation of submarine massive sulfide mounds (Iberian Pyrite Belt), Miner. Depos., 54, 913-934, 10.1007/s00126-018-0853-x, 2019.

S1.2 History of Aguas Teñidas mine

The eastern sector of Aguas Teñidas deposit (named Aguas Teñidas Este) was discovered in 1985 when a survey in the area around the old Aguas Teñidas Mine by Billiton Española S.A. and Promotora de Recursos Naturales showed a strong electro-magnetic anomaly 2 km east of the old mine, and subsequent exploratory drilling of the area intersected the massive sulphides in the third hole. Billiton Española S.A. delineated the deposit with 32 holes produced from 1985 to 1990. In 1990 the company relinquished the property, which was then acquired by Placer Dome Inc. in 1991. This company continued exploration drilling between 1991 and 1994, further delineating the deposit and the associated stockwork with 27 new holes. Navan Resources PLC acquired the property in 1995, construction of a ramp to reach the massive sulphides began in 1997, and the deposit was hit in early 1999. Finally, production began in late 1999 (Hidalgo et al., 2000). However, after only 3 years of production the mine closed due to low metal prices. In 2005, with metal values rising again, Iberian Minerals Corp. bought the mining rights and presented a project for reopening the mine. In 2006 the project was approved, and in 2009 commercial mining started again with an initial production of 1.7 Mt/year. Several processing plant expansions since 2009 have risen the production potential to 4.6 Mt/year (2015) (MATSA website). During this last stage, further exploration of the deposit led to the discovery of the Western Extension, which is the west-ward continuation of Aguas Teñidas Este and occurs below the old Aguas Teñidas Mine.

References

Hidalgo, R., Guerrero, V., Pons, J. M., and Anderson, I. K.: The Aguas Teñidas Este mine, Huelva Province, SW Spain, 2000.

S1.3 Portable XRF assessment and calibration

Prior to standard or sample analysis, an assessment was made on the effect of equipment warm-up, measuring time, distance to sample, water content, and number of analysis per sample.

Assessment of warm-up effect

Equipment warming-up can have a significant effect on the measured intensities, especially of light elements (e.g. SiO_2, K_2O, Al_2O_3) (Gallhofer and Lottermoser, 2018). This effect is higher during the initial warm-up at the beginning of the measurement session, when the largest temperature rise occurs, and is lower during slower subsequent warm-up along the session (Steiner et al., 2017; Gallhofer and Lottermoser, 2018). Gallhofer and Lottermoser (2018) used a Bruker S1 Titan p-XRF, for which a 30 min warm-up time was established for measurements stabilization at the beginning of each session.

To evaluate the effect of warm-up in our Thermo NITON XL3t 900Analyzer with GOLDD, a sample in the form of pressed powder pellet was repeatedly measured using the Standard soil program over a 1:15 h interval starting from cold conditions. Then, the equipment was allowed to cool down for 30 min before measuring again to check if cooling for a period of time which could elapse in normal operating conditions in mineral exploration had a significant effect. Results are shown in Fig. S1.

An increase in measured concentrations is seen during the first 15 min, upon which concentrations in the range of the following measurements are attained. Since this measuring program does not analyse light elements, an additional safety margin was considered based on the results by Gallhofer and Lottermoser (2018). Thus, at the beginning of each session 20 minutes of continuous measurements were performed for equipment warm-up and stabilization.

The 30 min cool-down period did not have a significant effect on measured concentrations.

Assessment of counting time

Counting time has a strong effect on measurement precisions (e.g. Hall et al., 2014; Bourke and Ross, 2015), and thus needs to be assessed.

Consecutive measurements were performed on the same spot of a pressed powder pellet, with 10, 20, 30 and 40 s counting time per filter for both Standard soil mode (3 filters) and Cu/Zn mining mode (4 filters). 15 analyses were made for each configuration, and relative standard deviations (RSD) were calculated (Fig. S2).

Results show a strong increase in precision from 10 to 20 s counting time, followed by lower increases at 30 and 40 s except for the elements with the lowest precisions (e.g. Sb, Ba, Mg). The lowest precisions are due to the light character of the element (e.g. Mg) and/or to its low content in the studied sample. These results are similar to those obtained by Hall et al. (2014) and Bourke and Ross (2015) on other p-XRF equipment, which showed only minor precision increase after 20-30s, and no precision increase beyond 60 s count time per filter.

Works studying the analytical capabilities of p-XRF and its use as a lithogeochemical characterization tool typically aim at high precisions, ideally close to those of lab-based equipment. For this purpose long measuring times are used (e.g. 60 s per filter or 200-240 s in total) to measure prepared samples (e.g. Conrey et al., 2014; Le Vaillant et al., 2014; McNulty et al., 2018, Hall et al., 2016). However, such long counting times are unpractical if the method is to be applied in real exploration situations on rock surfaces or hand specimens. 60 s per filter counting time involves 3 min-long acquisition times in the Standard soil mode (3 filters) and 4 in the Cu/Zn mining mode (4 filters); 7 minutes per spot in total if both filters are used.

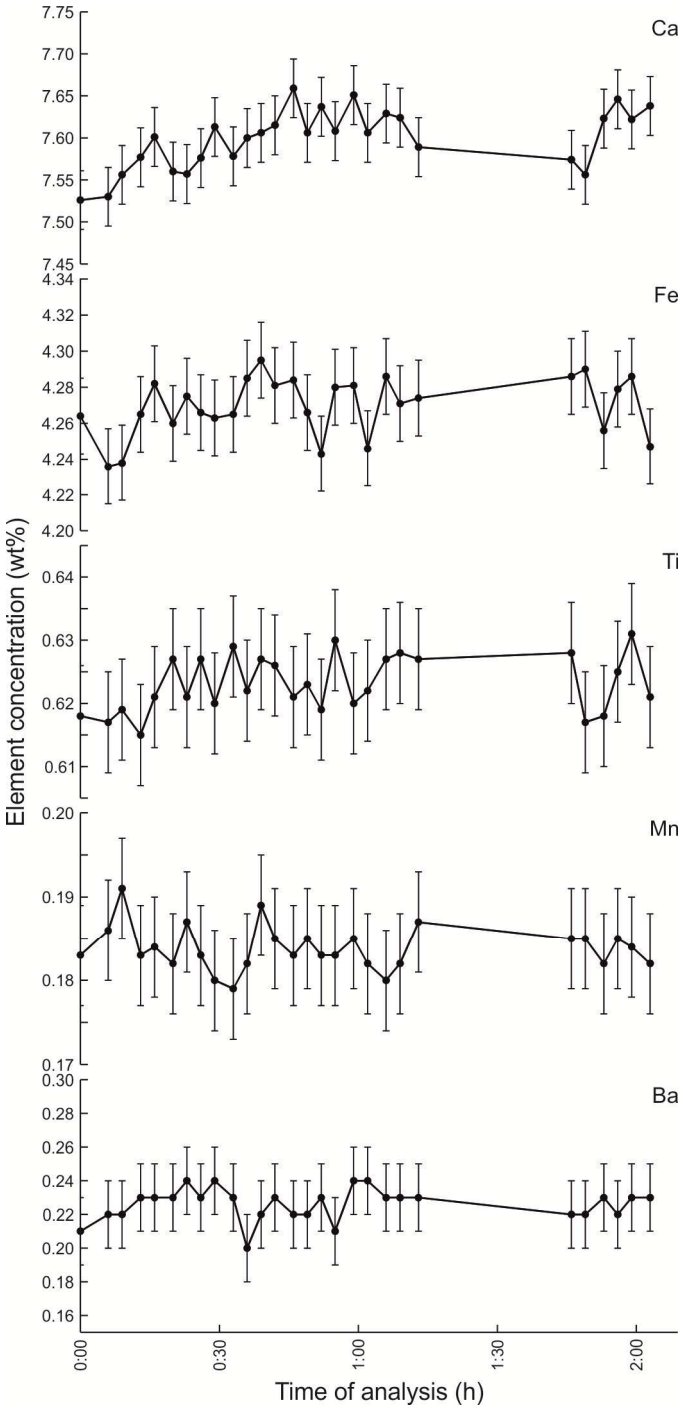

Figure S1. Element concentrations during p-XRF warm-up. Error bars correspond to 2 standard deviations (SD) as provided by the equipment in the analytical results output.

Since the characterization of hand specimens requires the analysis of several spots per sample (at least 3; Hall et al., 2014; Ross et al., 2014), this would add to 10 to 20 minutes measuring time, which is unrealistic. Therefore, in this study a counting time of 30 s per filter, equivalent to that used in other exploration studies (e.g. Ross et al., 2014, 2016; Duée et al., 2019), was chosen as a compromise between precision and convenience to keep the analysis time at 2 minutes; we consider this amount of time as reasonable for a hand-held device. Although 30 s per filter were used on this study, based on results in Fig. S2, we suggest that 20 s counting times could also provide sufficiently accurate results if reduced measuring times were needed.

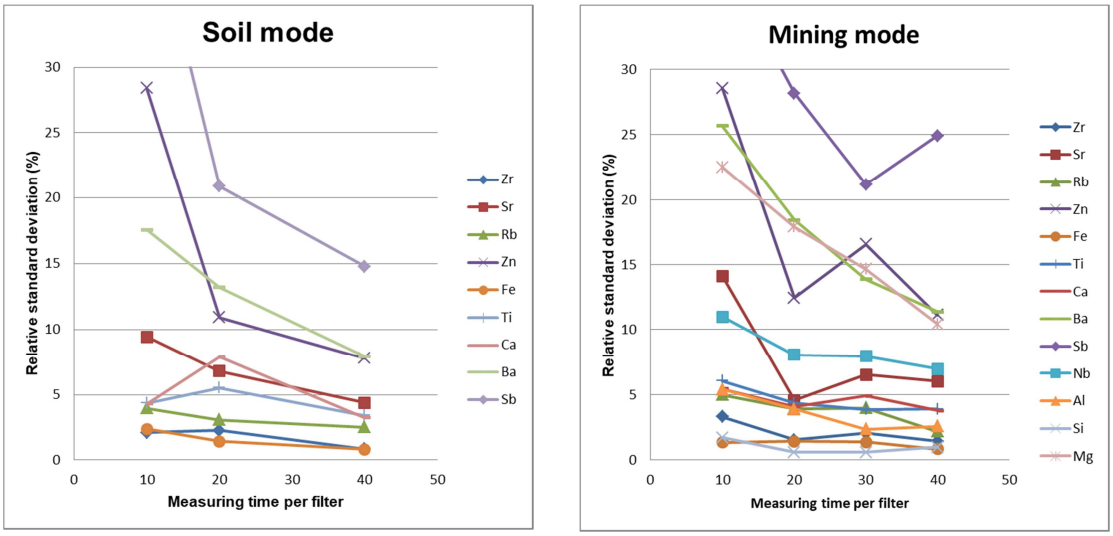

Figure S2. Relative standard deviation for each element at different counting times in both soil and mining mode.

Selection of the measuring program

Two main analysis programs can be used in the NITON XL3t 900Analyzer with GOLDD for the analysis of rocks for exploration purposes (e.g. Duée et al., 2019): the Standard soil mode and Cu/Zn mining mode.

The Standard soil mode is mainly used for the analysis of contaminants in soils. It is optimized for light matrices (e.g. aluminium silicates), elements of interest in concentrations < 1wt %, and elements with atomic number higher than Fe not exceeding several wt %. This mode utilizes Compton Scatter (inelastic collisions) to approximate element concentrations.

The Cu/Zn mining mode is optimized for testing soils and rocks without adjusting for a particular matrix, and is intended primarily for the detection of metal concentrations in light matrices. This mode utilizes Fundamental Parameters to approximate element concentrations. It performs better for samples whose elements of interest are in concentrations > 1 wt %, but the FP algorithm accurately measures elemental concentrations from trace levels to 100 wt %, and automatically corrects for inter-element effects.

The elements measured depend on the program used. The Standard soil mode includes Mo, Zr, Sr, U, Rb, Th, Pb, Au, Se, As, Hg, Zn, W, Cu, Ni, Co, Fe, Mn, Cr, V, Ti, Sc, Ca, K, S, Ba, Cs, Te, Sb, Sn, Cd, Ag, Pd. From this, U, Th, Hg, Sc, Cs and Te are not available in the Cu/Zn mining mode. On the other hand, the Cu/Zn mining mode includes Nb, Bi, Al, P, Si, Cl, Mg.

Many exploration studies use two analytical modes (e.g. Le Vaillant et al., 2014; Hall et al., 2016; Ross et al., 2016) to optimize analytical precision and detected limits for all elements of interest. However, in this study, for analytical convenience during active exploration it was decided to use only one test mode at each spot. Although during testing the soil mode showed better detection limits for base metals, the use of the Cu/Zn mining mode was chosen because it includes light elements, which can be of importance during alteration halo investigation, and Nb and Al, which are important for lithological unit recognition, as detailed in the main text.

Assessment of the number of analysis

One of the aims of this study is to evaluate the usefulness of direct p-XRF analysis of natural rocks for ore exploration. Thus, the use of highly prepared samples (e.g. pressed pellets of rock powder) was not considered. Rocks are naturally

heterogeneous at small scales due to factors such as compositional variations along the rock (e.g. changes in sediment composition from layer to layer) or grain size (e.g. different minerals in coarse-grained igneous rocks). Given the limited area of the spots analysed by p-XRF equipment (typically around 8 mm in diameter), the composition of several spots needs to be averaged to approximate the actual whole rock composition of the studied sample.

Previous studies suggest that 3 analyses already provide a good approximation, with the main gain in precision occurring until 7 analyses (Bourke and Ross, 2015). These can be closely-spaced analysis to characterize a specific sample or rock fragment (e.g. Conrey et al., 2014; Hall et al., 2014; McNulty et al., 2018), or more separated spots in broader downhole systematic drill core studies (e.g. three-point moving average, Ross et al., 2014, 2016). In the current study, the porphyritic or coarse clastic character of most of the studied lithologies, combined with the nugget effect of mineralization in the VMS hydrothermal system, required an independent analysis to assess the optimum number of spots to analyse on each sample.

A precision test based on that of Bourke and Ross (2015) was performed. Two samples (AM-49/879.75 and AE-68/101.8) were analysed using the Cu/Zn mining mode at 30 s per filter. At least 20 randomly distributed points were analysed on each sample on the flat surface obtained from sawing the drill core in two halves. In addition, on sample AE-68/101.8 the rougher curved drill core surface was also analysed. For each set of analysis average compositions were calculated using random subgroups of 2 to 15 analyses each; 100 averages were calculated for each subsample size (i.e. 100 averages for subgroups of 2 analyses, 100 averages for subgroups of 3 analyses, and so on). Standard deviation and relative standard deviation was then calculated for the averages obtained for each subsample size. Results are presented in Figure S3.

The largest decrease in RSD occurs from 1 to 4 analyses per average, and the trend nearly flattens out after 8 analyses per average. Precisions obtained from the analysis of the cut surface in sample AE-68/101.8 are lower because of the presence of two outlier analyses; these can be seen in Figure 9 in the main text.

Previous works suggest that averaging 3 analyses is usually enough to obtain representative average whole rock compositions. Based on our results, we suggest that 5 to 7 analyses should be used, and we have used 7 of them during the development of this study in order to work with RSD usually better than 10 % for all elements, and to minimize the effect of outliers such as those analysed in AE-101.8 and the nugget effect in lightly mineralized samples (e.g. Bourke and Ross, 2015). In porphyritic, hydrothermally altered, tectonically deformed and metamorphosed rocks with variable occurrence of multiple generations of hydrothermal and metamorphic veins like those investigated in this work, presence of chemical outliers is common and needs to be considered.

Point averaging can be performed during analysis or afterwards during data processing. Devices such as the Thermo NITON XL3t 900Analyzer include analysis options which automatically calculate and present average compositions obtained from n consecutive analyses, with n set by the user. If the device is configured with user custom calibration factors, this tool may provide final lithogeochemical results on site, which can be highly useful in settings such as during active field exploration.

Effect of distance to sample

During real exploration conditions, access to flat smooth rock surface for analysis is rare. Usually rough (natural rock surfaces) or curved (drill core surface) surfaces are the only available to be analysed. Besides other effects such as refraction and diffraction, studied by works such as Duée et al. (2019), surface irregularity produces an increase in the average distance between the sample and the detector, and the occurrence of the analysed surface away from the ideal focal distance to the detector (Laperche and Lemière, 2021). The effect of this distance on the measured intensity and calculated concentration of the analysed elements has been studied to assess their consequences when using element concentrations or elemental ratios during exploration.

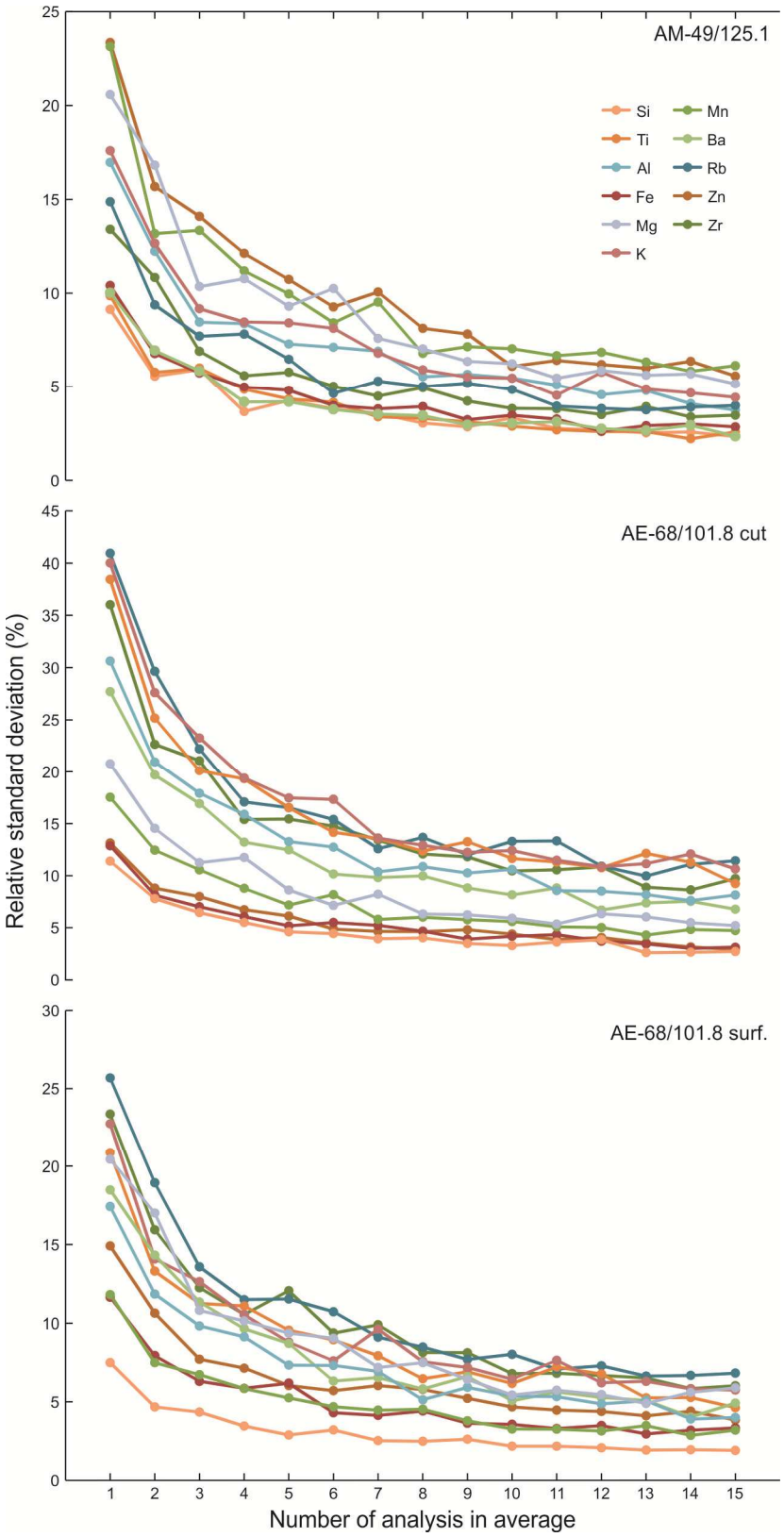

Figure S3. Relative standard deviations for average element concentrations calculated for subsamples of different sizes (1 to 15 random analyses per average).

Two pressed powder pellets were repeatedly analysed on the same spot at increasing distances from the front of the p-XRF, up to 3.5 mm. Using the initial composition at zero distance (pellet in contact with the equipment) as a reference, relative decreases in concentration were calculated. Results for some elements of interest are shown in Figure S4.

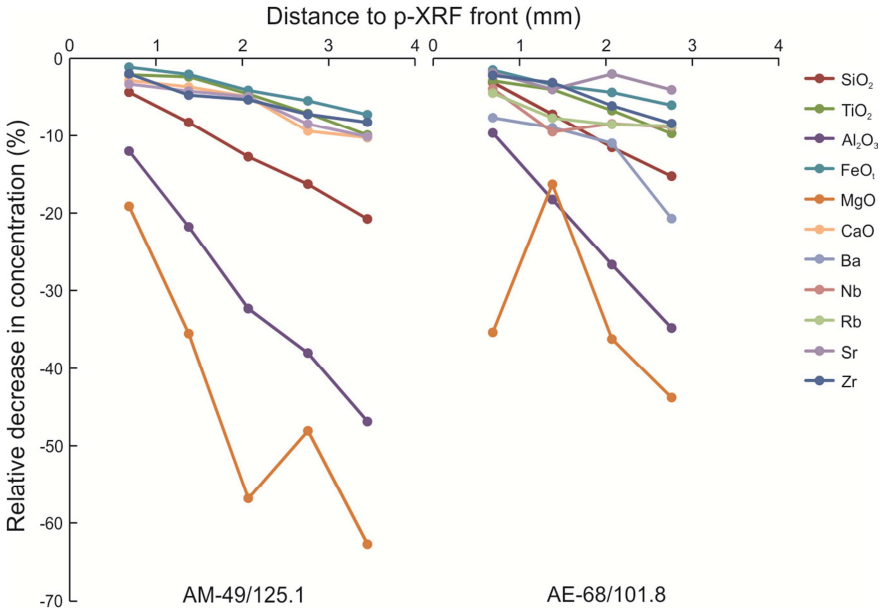

Figure S4. Relative decreases in concentration with changing distance from sample to p-XRF.

Concentration changes show a clear correlation with the atomic number of the elements; these are higher for light elements, especially Mg, Al and Si, and lower for heavier elements. For heavier elements, within the studied distance range concentration changes remain below 10 %, whereas for light elements they can be in excess of 60%.

Thus, it needs to be taken into account that irregular surfaces will produce variable modifications in concentrations depending on the atomic number of the elements, which therefore cannot be corrected to the original values through simple normalization; and also on element ratios, which can be used for lithological unit identification, exploration or other lithogeochemical characterizations (e.g. Conrey et al., 2014; Ross et al., 2014). Ratios between heavy and light elements (e.g. Zr/Al) will undergo larger changes than ratios between elements of more similar behaviour (e.g. Zr/Ti).

Effect of water

During regular exploration, analysis conditions are typically far from ideal laboratory conditions. Samples to be analysed can be dusty or wet, and cannot be thoroughly cleaned and dried in an oven prior to analysis. At most, the surface can be cleaned with a damped cloth or running water and be left briefly to dry. Therefore, the effect of moisture or dampness of rock samples on p-XRF analysis needs to be evaluated. Water causes x-ray scatter and absorption, inducing an increase in the scattered x-rays in the fluorescence spectrum and a decrease in the intensity of characteristic x-rays of the elements. Previous works (e.g. Ge et al., 2005; Bastos et al., 2012) have studied signal behaviour on soil samples. But as far as we are aware, no systematic studies have been made on rock samples.

Thus, the effect of water on rock samples has been evaluated here by analysing two samples under several conditions. Sample AGI-888/173.5 corresponds to chloritized host rock by the upper contact of the massive sulphides. Sample AGI-888/180.9 is hanging wall red shale collected some metres above the massive sulphides. Both specimens were sampled within the hanging wall geochemically anomalous halo related to the ore, which is described in the main text. These samples, like most studied in this work, correspond to metamorphic rocks with a low permeability. Thus, results shown next cannot be directly extrapolated to rocks in other study areas.

On each sample the same spot was measured twice 1) after overnight sample drying at 70°C; 2) after moisturizing the sample surface with a wet cloth simulating sample cleaning and allowing some seconds for the surface to dry; 3) after immersion of the sample in water for 5 minutes simulating more intensive sample cleaning; in this case excess water on sample surface

was removed with a dry cloth immediately prior to analysis. In sample AGI-888/180.9 an additional analysis was performed on the sample with a water-soaked surface. Results are provided in Table S1.

	Major elements (wt %)							
	SiO_2	TiO_2	Al_2O_3	FeOt	MnO	MgO	CaO	K_2O
AGI-888/173,5								
Oven 1	43.04	0.45	34.60	7.62	0.52	17.22	0.26	3.10
Oven 2	43.50	0.45	34.29	7.65	0.51	15.85	0.14	2.91
Wiped 1	43.94	0.36	30.88	7.74	0.50	7.90	0.12	3.00
Wiped 2	43.90	0.31	31.19	7.74	0.50	8.39	0.12	2.98
Immersed 1	44.10	0.35	30.40	7.76	0.51	7.86	0.12	2.94
Immersed 2	43.16	0.36	33.97	7.83	0.50	16.30	0.12	2.98
AGI-888/180.9								
Oven 1	59.17	0.39	18.66	5.09	0.16	2.87	0.40	2.30
Oven 2	58.72	0.37	18.44	5.04	0.16	2.76	0.41	2.28
Wiped 1	59.79	0.40	19.08	5.02	0.16	3.29	0.41	2.30
Wiped 2	59.40	0.37	18.60	5.00	0.17	3.66	0.40	2.28
Immersed 1	59.29	0.37	18.84	4.99	0.17	2.98	0.39	2.28
Immersed 2	59.67	0.36	18.47	4.97	0.16	2.70	0.37	2.24
Soaked 1	37.21	0.32	5.87	4.67	0.15	< d.l.	0.32	1.89
Soaked 2	39.92	0.35	7.13	4.93	0.16	0.66	0.33	2.07

	Trace elements (ppm)												
	As	Ba	Cr	Cu	Nb	Pb	Rb	Sb	Sn	Sr	V	Zn	Zr
AGI-888/173,5													
Oven 1	<d.l	4355	243	149	41	82	123	< d.l.	40	348	212	457	612
Oven 2	<d.l	4456	237	127	34	57	116	< d.l.	35	338	175	420	619
Wiped 1	<d.l	4612	193	130	31	37	109	< d.l.	28	335	84	445	622
Wiped 2	<d.l	4558	190	127	29	39	102	< d.l.	29	340	249	429	627
Immersed 1	<d.l	4577	218	140	35	43	110	< d.l.	33	335	224	423	624
Immersed 2	<d.l	4532	212	124	31	39	109	< d.l.	35	338	164	420	624
AGI-888/180.9													
Oven 1	108	2055	25	< d.l.	16	43	106	88	< d.l.	207	57	220	341
Oven 2	108	2000	28	< d.l.	16	43	104	80	< d.l.	211	59	227	337
Wiped 1	110	2026	23	< d.l.	17	45	109	77	< d.l.	211	45	207	347
Wiped 2	114	2066	24	< d.l.	17	46	106	88	< d.l.	211	41	214	346
Immersed 1	104	2010	37	< d.l.	16	49	108	84	< d.l.	209	37	222	340
Immersed 2	108	1999	33	< d.l.	17	46	108	80	< d.l.	208	35	229	342
Soaked 1	101	1963	17	< d.l.	17	50	103	80	< d.l.	206	51	204	336
Soaked 2	104	2064	38	< d.l.	17	46	106	85	< d.l.	204	61	229	345

Table S1. Results of the analysis of two samples under different moisture conditions

Results show no significant effect, even when analysing through a thin film of water, for elements with high atomic number (trace elements). Effect on Ti and Fe is minor, only observable under soaked conditions. On the other hand, moisture and water can have an important effect on lighter elements. Ca, K and Si show a significant decrease in measured concentrations under soaked conditions, although not in less wet settings. The lightest analysed elements, Al and Mg, also show a decrease in measured concentrations if the sample surface is moist. This is more marked in sample AGI-888/173.5, maybe due to higher porosity retaining more water. However, under each condition, the second analysis (finished 2 minutes after the first one) yields higher concentrations, showing the effect of progressive surface drying. These results are consistent with those of Ge et al. (2005), who described a significant influence of water on elements with atomic number < 26, with larger attenuation of lower energies (lighter elements) (Bastos et al., 2012).

These results show that, as long as the surface of the sample is dry, results obtained are valid except for the lightest elements (Al, Mg), even if the rock was originally soaked in water and its interior is still moist. Given that the lightest elements, on which moisture may have a stronger effect, are measured from the most surficial portions of the sample (Ravansari et al., 2020), allowing some time for visible surface drying should be enough to provide good quality analyses, without the need for thorough sample drying. Additionally, we consider that obtained data make complex spectrum-based post-processing corrections of the water effect (e.g. Ge et al., 2005; Bastos et al., 2012, implemented for water contents up to 20 wt % in soil samples) unnecessary in the analysis of samples similar to those studied here.

Equipment calibration

Matrix plays an important effect on XRF measurements. Thus, it is recommended to prepare custom calibration lines using samples with characteristics as close as possible to the samples to be analysed. The aim of the p-XRF part of this study is to analyse rock samples either in the lab or directly in the field or on the drill core. Since attempting calibration using hand specimens of known whole rock composition is unrealistic, the use of pressed powder pellets was chosen as the most similar approximation to rock samples, but with the advantage of homogeneous known composition and flat smooth surface. Pressed pellets were used instead of powder cups because loose powdered samples lose much more intensity from internal scattering compared to denser solids (Conrey et al., 2014). In addition, powder cups have a plastic film which is not present during rock sample analysis. To match the matrix of our samples the use of commercial standards was ruled out and pellets were prepared using powdered samples collected, prepared and analysed for whole rock geochemistry at SGS during this study. Pellets were prepared with 15 g of sample pressed at 200 kN for 2 minutes with no binding materials such as resin or wax, as these could introduce modifications into the measured signal.

To cover the whole compositional range in the studied area, and to minimize the effect of analytical precision and accuracy both from laboratory and p-XRF analyses in the calculated calibration lines, a relatively large number of samples was used for calibration. 15 samples representative of all lithologies and compositions of Aguas Teñidas, plus 2 additional shale samples from the southern IPB were prepared into pellets and used for calibration.

Each pellet was analysed using the Cu/Zn mining mode with 30 s measuring time per filter on 5 different spots to minimize the influence of measurement precision and possible nugget effects due to incomplete sample homogenization during powdering.

Analytical results provide some constraints on the usefulness of the calculated calibration lines. For example, samples with P_2O_5 < 0.15 wt % (most of the analysed samples) produce no valid results upon analysis with the used p-XRF equipment. The same occurs for As < 20 ppm, Cr < 75 ppm, Cu < 50 ppm, Pb < 100 ppm, V < 50 ppm. For Ba, analysed concentrations depict a nearly two-point calibration line, with most samples < 600 pm, and few samples reaching up to 7500 ppm. During this study a single calibration line has been used, but for higher accuracy two calibration lines could be calculated, for samples below and above 1000 ppm respectively. The use of trimmed calibration lines for the low-concentration range of several elements has been suggested in previous studies (e.g. Hall et al., 2014).

Most p-XRF devices allow configuration of user custom calibration factors, thus providing analytical results which require no subsequent processing for concentration corrections. In this case, a single calibration factor is used for each element.

References

Bastos, R. O., Melquiades, F. L., and Biasi, G. E. V.: Correction for the effect of soil moisture on in situ XRF analysis using low-energy background, X-Ray Spectrometry, 41, 304-307, 10.1002/xrs.2397, 2012.

Bourke, A., and Ross, P.-S.: Portable X-ray fluorescence measurements on exploration drill-cores: comparing performance on unprepared cores and powders for 'whole-rock' analysis, Geochemistry: Exploration, Environment, Analysis, 16, 147-157, 10.1144/geochem2014-326, 2015.

Conrey, R. M., Goodman-Elgar, M., Bettencourt, N., Seyfarth, A., Van Hoose, A., and Wolff, J. A.: Calibration of a portable X-ray fluorescence spectrometer in the analysis of archaeological samples using influence coefficients, Geochemistry: Exploration, Environment, Analysis, 14, 291-301, 10.1144/geochem2013-198, 2014.

Duée, C., Orberger, B., Maubec, N., Laperche, V., Capar, L., Bourguignon, A., Bourrat, X., El Mendili, Y., Chateigner, D., Gascoin, S., Le Guen, M., Rodriguez, C., Trotet, F., Kadar, M., Devaux, K., Ollier, M., Pillière, H., Lefèvre, T., Harang, D., Eijkelkamp, F., Nolte, H., and Koert, P.: Impact of heterogeneities and surface roughness on pXRF, pIR, XRD and Raman analyses: Challenges for on-line, real-time combined mineralogical and chemical analyses on drill cores and implication for "high speed" Ni-laterite exploration, J. Geochem. Explor., 198, 1-17, https://doi.org/10.1016/j.gexplo.2018.12.010, 2019.

Gallhofer, D., and Lottermoser, B. G.: The Influence of Spectral Interferences on Critical Element Determination with Portable X-Ray Fluorescence (pXRF), Minerals, 8, 320, 2018.

Ge, L., Lai, W., and Lin, Y.: Influence of and correction for moisture in rocks, soils and sediments on in situ XRF analysis, X-Ray Spectrometry, 34, 28-34, 10.1002/xrs.782, 2005.

Hall, G. E. M., Bonham-Carter, G. F., and Buchar, A.: Evaluation of portable X-ray fluorescence (pXRF) in exploration and mining: Phase 1, control reference materials, Geochemistry: Exploration, Environment, Analysis, 14, 99-123, 10.1144/geochem2013-241, 2014.

Hall, G. E. M., McClenaghan, M. B., and Pagé, L.: Application of portable XRF to the direct analysis of till samples from various deposit types in Canada, Geochemistry: Exploration, Environment, Analysis, 16, 62-84, 10.1144/geochem2015-371, 2016.

Laperche, V., and Lemière, B.: Possible Pitfalls in the Analysis of Minerals and Loose Materials by Portable XRF, and How to Overcome Them, Minerals, 11, 33, 2021.

Le Vaillant, M., Barnes, S. J., Fisher, L., Fiorentini, M. L., and Caruso, S.: Use and calibration of portable X-Ray fluorescence analysers: application to lithogeochemical exploration for komatiite-hosted nickel sulphide deposits, Geochemistry: Exploration, Environment, Analysis, 14, 199-209, 10.1144/geochem2012-166, 2014.

McNulty, B. A., Fox, N., Berry, R. F., and Gemmell, J. B.: Lithological discrimination of altered volcanic rocks based on systematic portable X-ray fluorescence analysis of drill core at the Myra Falls VHMS deposit, Canada, J. Geochem. Explor., 193, 1-21, https://doi.org/10.1016/j.gexplo.2018.06.005, 2018.

Ravansari, R., Wilson, S. C., and Tighe, M.: Portable X-ray fluorescence for environmental assessment of soils: Not just a point and shoot method, Environment International, 134, 105250, https://doi.org/10.1016/j.envint.2019.105250, 2020.

Ross, P.-S., Bourke, A., and Fresia, B.: Improving lithological discrimination in exploration drill-cores using portable X-ray fluorescence measurements: (2) applications to the Zn-Cu Matagami mining camp, Canada, Geochemistry: Exploration, Environment, Analysis, 14, 187-196, 10.1144/geochem2012-164, 2014.

Ross, P.-S., Bourke, A., Mercier-Langevin, P., Lépine, S., Leclerc, F., and Boulerice, A.: High-Resolution Physical Properties, Geochemistry, and Alteration Mineralogy for the Host Rocks of the Archean Lemoine Auriferous Volcanogenic Massive Sulfide Deposit, Canada, Economic Geology, 111, 1561-1574, 10.2113/econgeo.111.7.1561, 2016.

Steiner, A. E., Conrey, R. M., and Wolff, J. A.: PXRF calibrations for volcanic rocks and the application of in-field analysis to the geosciences, Chem. Geol., 453, 35-54, https://doi.org/10.1016/j.chemgeo.2017.01.023, 2017.

S1.4 Drill core columns

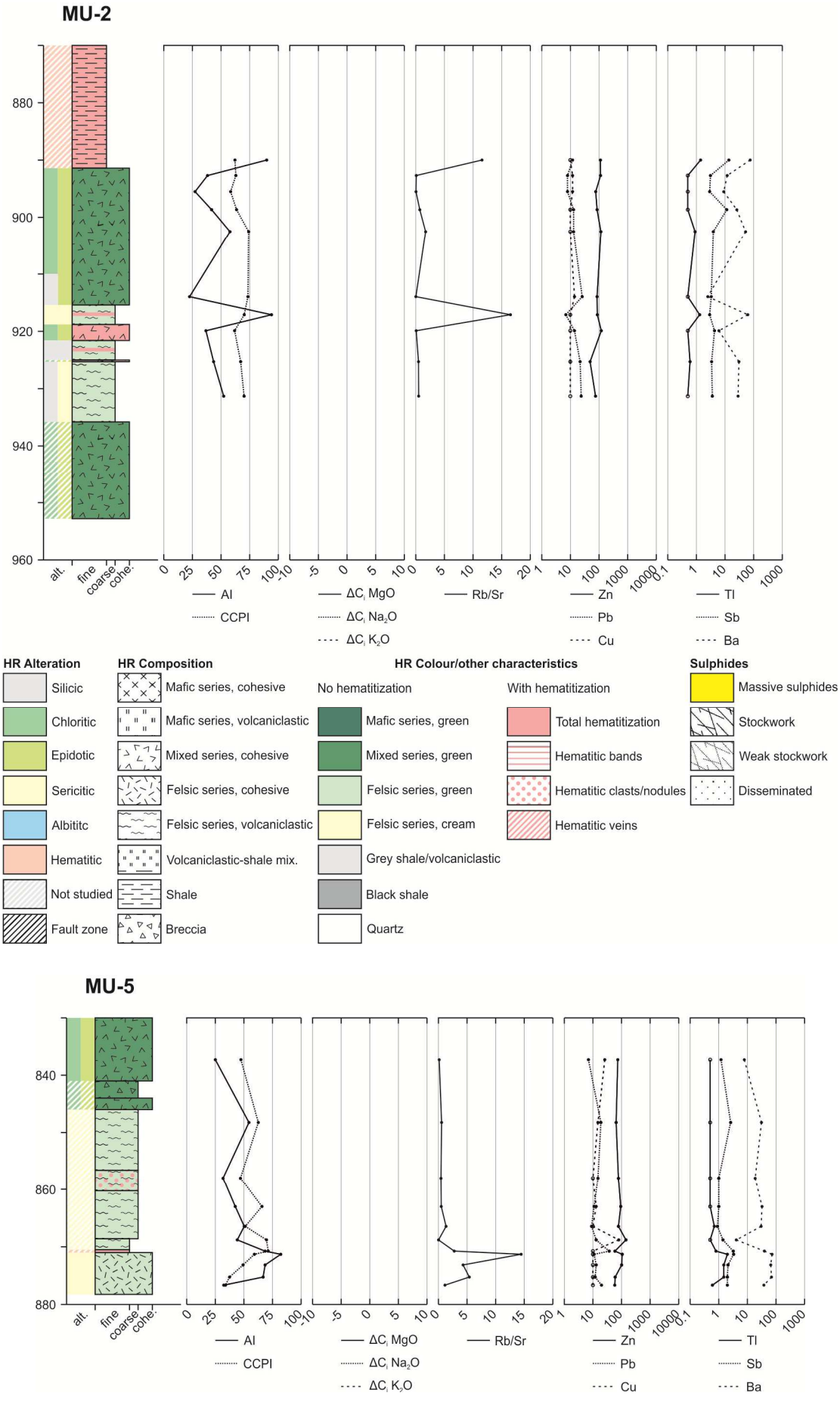

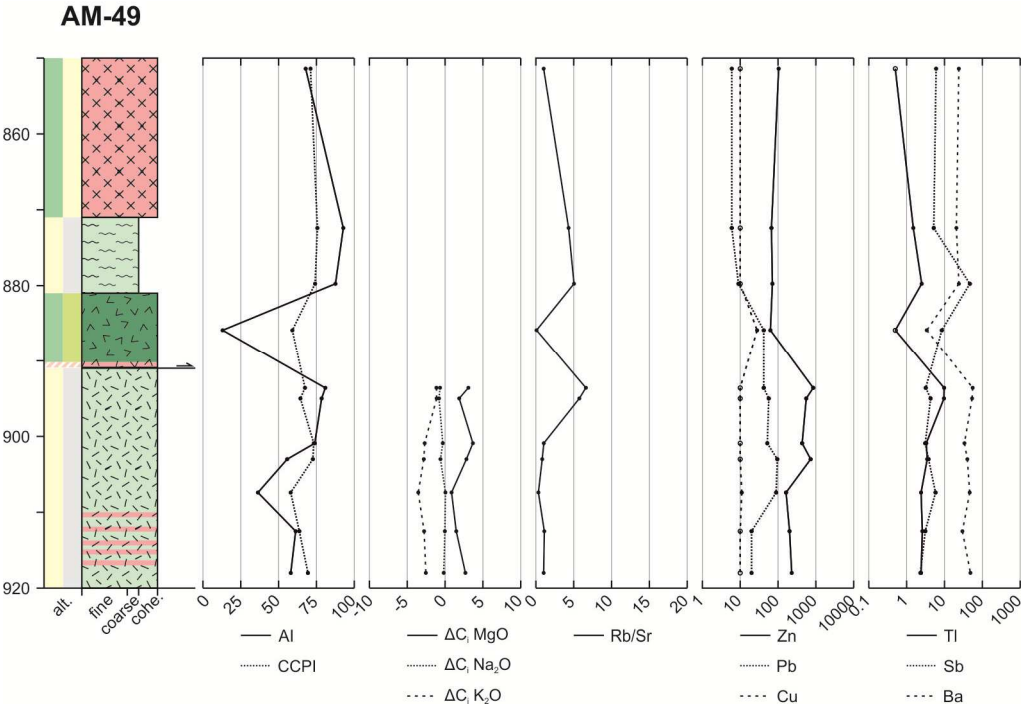
AM-49
860
880
900
920
alt.
fine
coarse
cohe.
0 25 50 75 100
-10 -5 0 5 10
0 5 10 15 20
1 10 100 1000 10000
0.1 1 10 100 1000
Al
CCPI
ΔC$_i$ MgO
ΔC$_i$ Na$_2$O
ΔC$_i$ K$_2$O
Rb/Sr
Zn
Pb
Cu
Tl
Sb
Ba

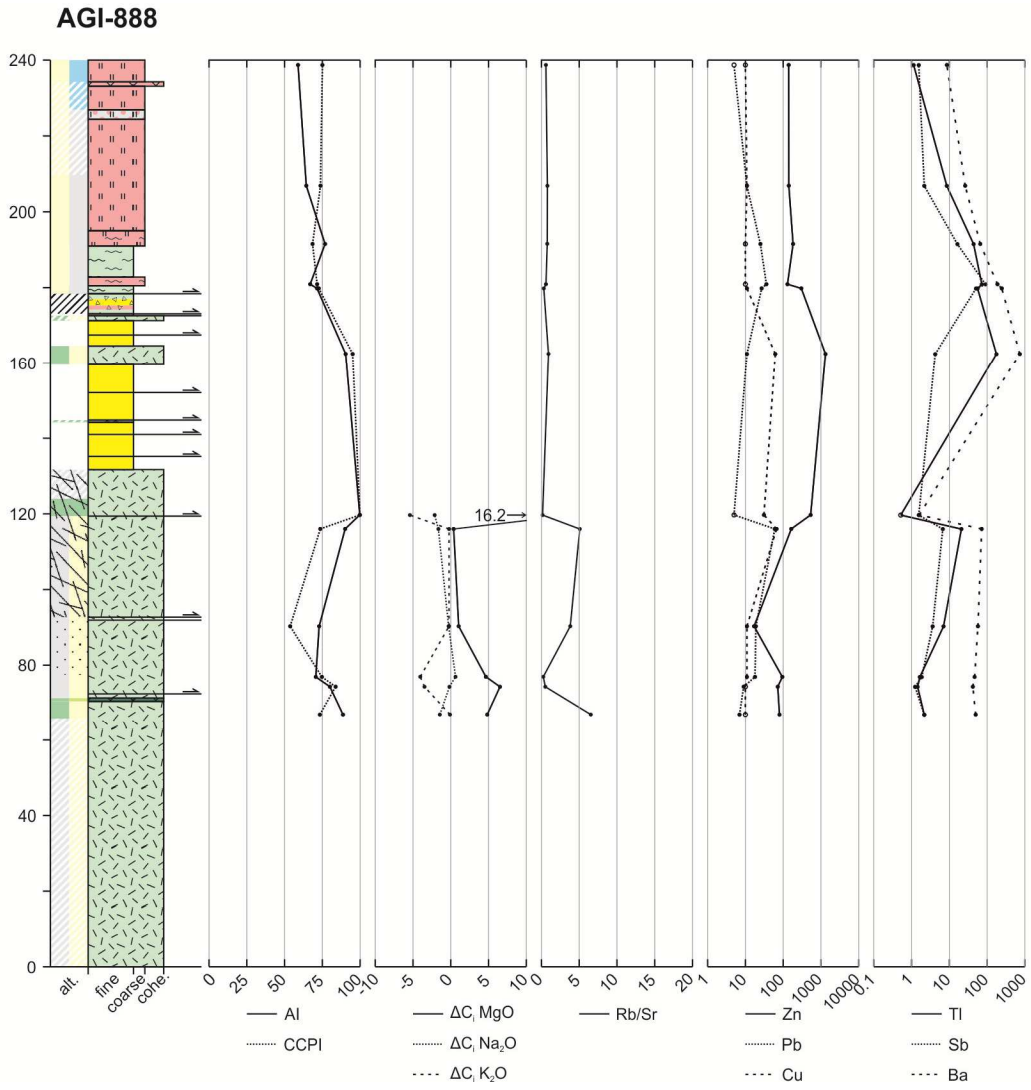
AGI-888
240
200
160
120
80
40
0
16.2
alt.
fine
coarse
cohe.
0 25 50 75 100
-10 -5 0 5 10
0 5 10 15 20
1 10 100 1000 10000
0.1 1 10 100 1000
Al
CCPI
ΔC$_i$ MgO
ΔC$_i$ Na$_2$O
ΔC$_i$ K$_2$O
Rb/Sr
Zn
Pb
Cu
Tl
Sb
Ba

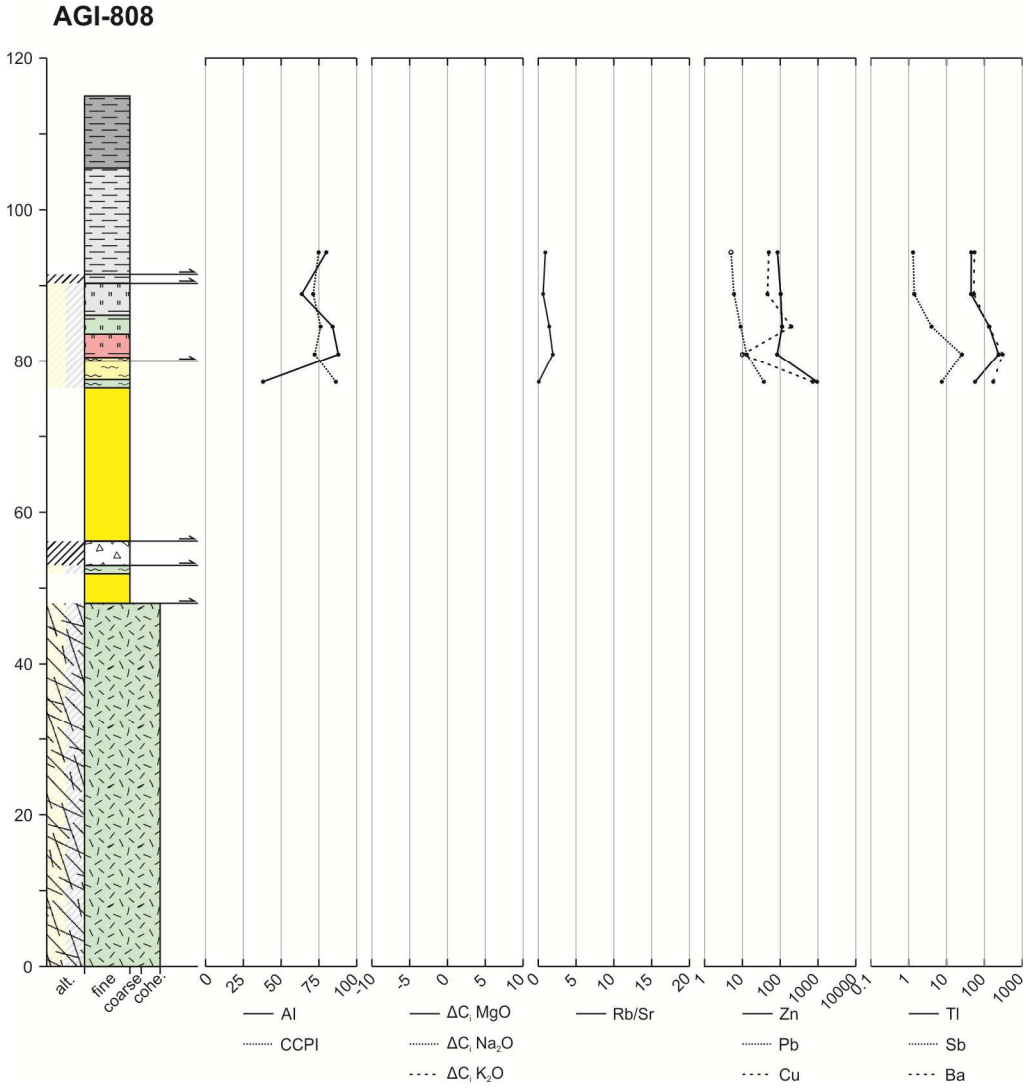
AGI-808
120
100
80
60
40
20
0
alt.
fine
coarse
cohe.
0
25
50
75
100
-10
-5
0
5
10
0
5
10
15
20
1
10
100
1000
10000
0.1
1
10
100
1000
AI
CCPI
ΔC$_i$ MgO
ΔC$_i$ Na$_2$O
ΔC$_i$ K$_2$O
Rb/Sr
Zn
Pb
Cu
Tl
Sb
Ba

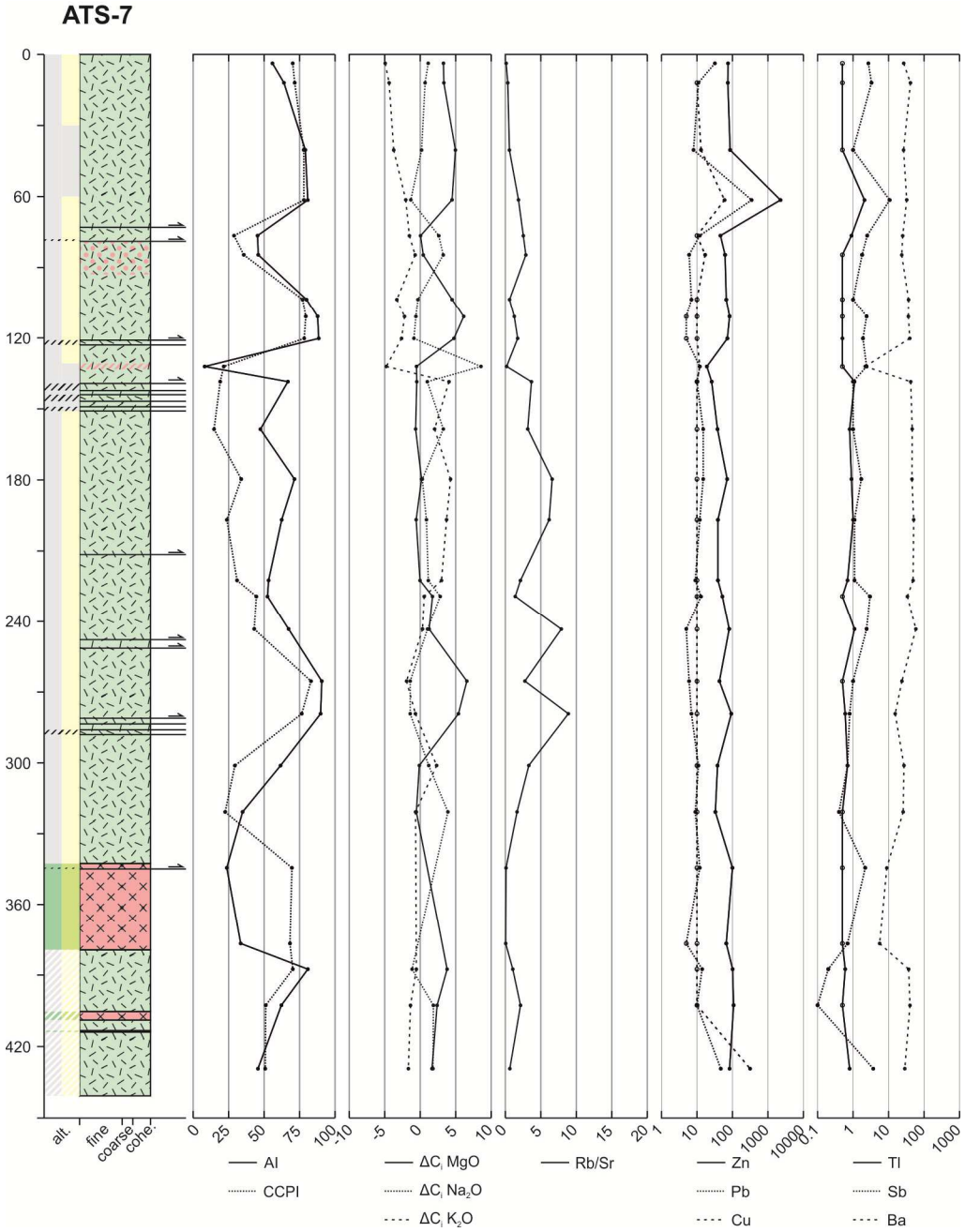
ATS-7
0
60
120
180
240
300
360
420
alt.
fine
coarse
cohe.
0
25
50
75
100
AI
CCPI
-10
-5
0
5
10
ΔCi MgO
ΔCi Na2O
ΔCi K2O
0
5
10
15
20
Rb/Sr
1
10
100
1000
10000
Zn
Pb
Cu
0.1
1
10
100
1000
Tl
Sb
Ba

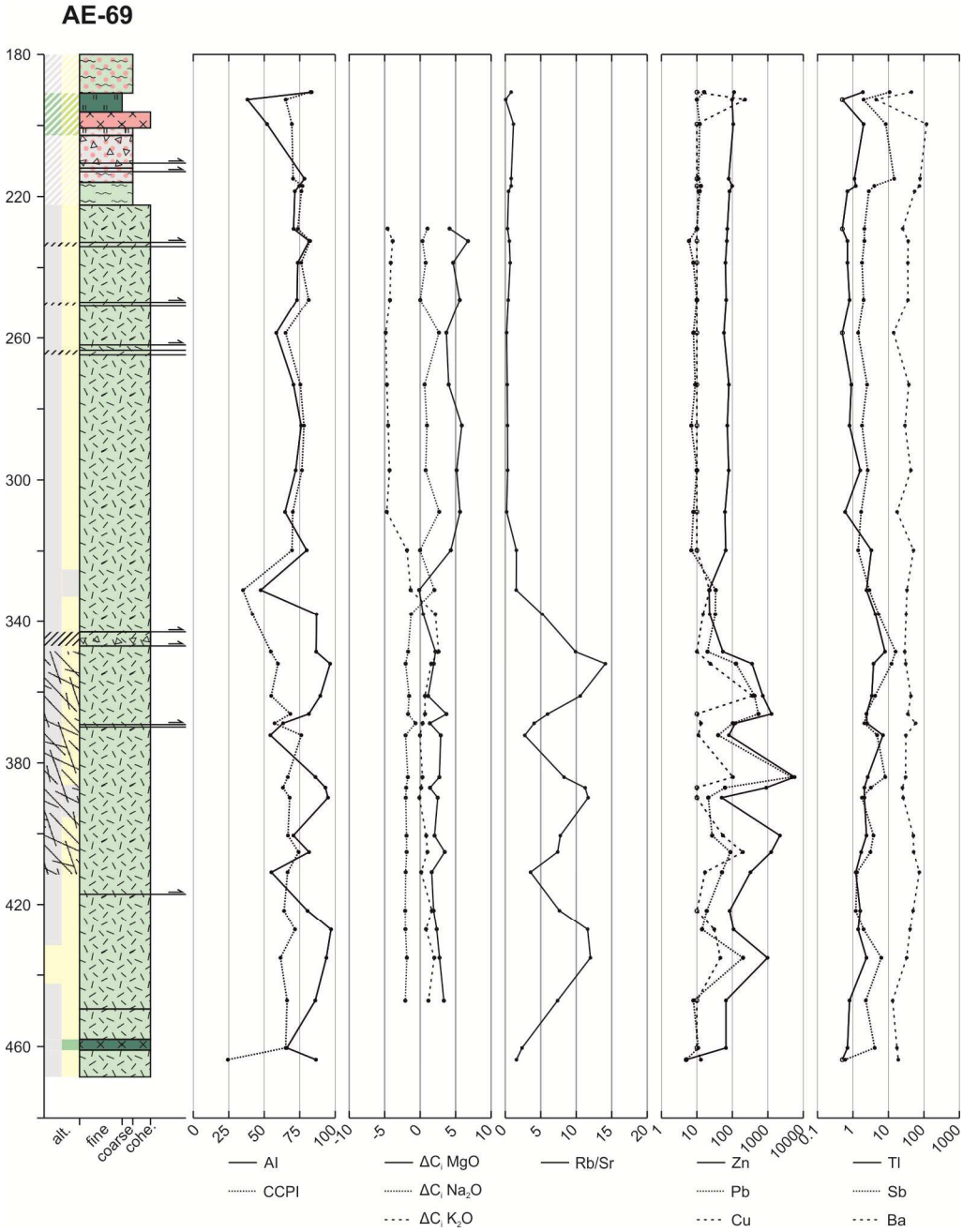
AE-69
180
220
260
300
340
380
420
460
alt.
fine
coarse
cohe.
0
25
50
75
100
-10
-5
0
5
10
0
5
10
15
20
1
10
100
1000
10000
0.1
1
10
100
1000
AI
CCPI
ΔC$_i$ MgO
ΔC$_i$ Na$_2$O
ΔC$_i$ K$_2$O
Rb/Sr
Zn
Pb
Cu
Tl
Sb
Ba

AE-68

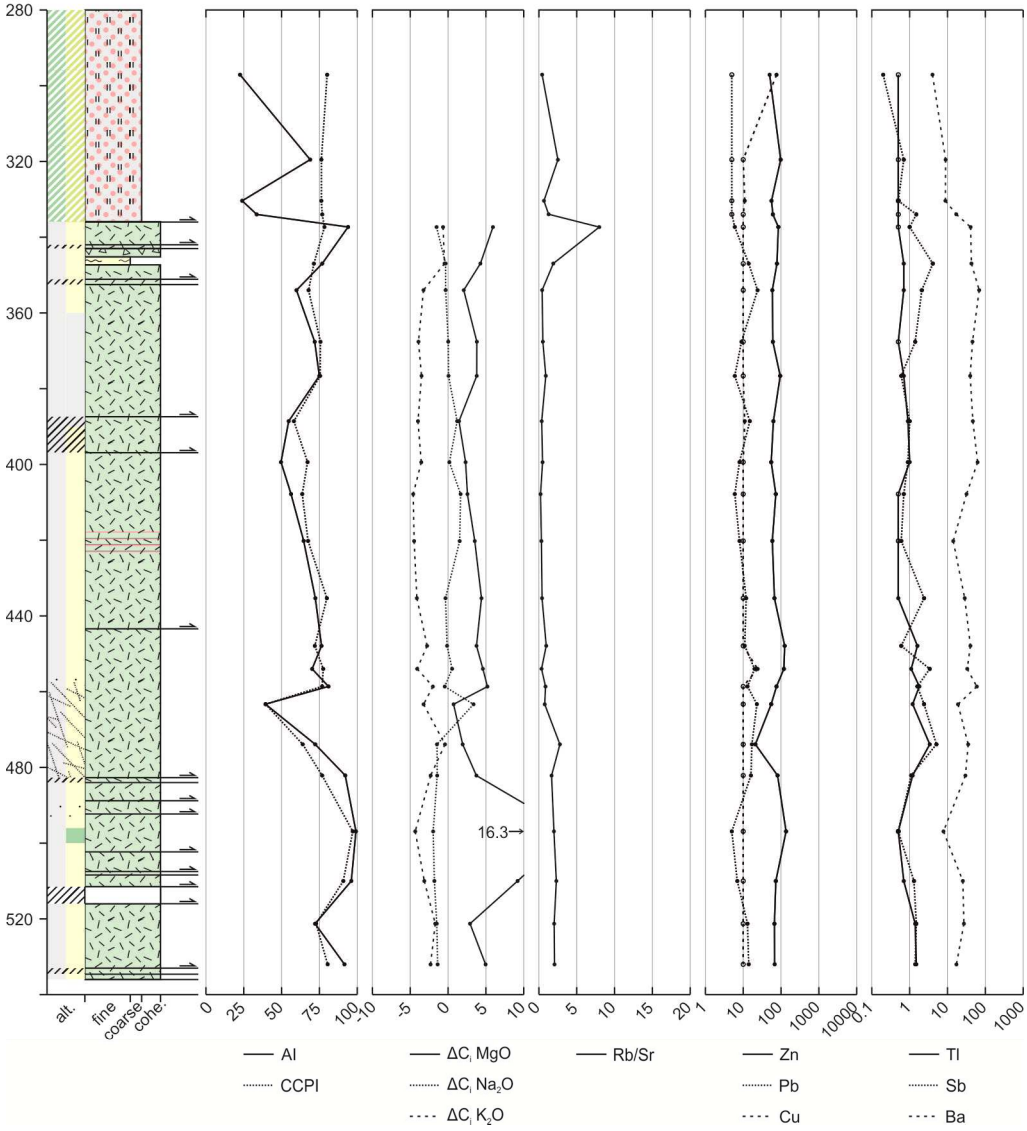
280
320
360
400
440
480
520
alt.
fine
coarse
cohe.
0
25
50
75
100
-10
-5
0
5
10
16.3
0
5
10
15
20
1
10
100
1000
10000
0.1
1
10
100
1000
AI
CCPI
ΔC$_i$ MgO
ΔC$_i$ Na$_2$O
ΔC$_i$ K$_2$O
Rb/Sr
Zn
Pb
Cu
Tl
Sb
Ba